



ELSEVIER

Earth and Planetary Science Letters 157 (1998) 41–56

EPSL

Mingling in mafic magma chambers replenished by light felsic inputs: fluid dynamical experiments

Roberto F. Weinberg¹, Alison M. Leitch^{*}

Research School of Earth Sciences, Australian National University, Canberra, ACT 0200, Australia

Received 7 April 1997; revised version received 12 January 1998; accepted 30 January 1998

Abstract

We investigate, by means of laboratory analogues, the fluid dynamics of magma hybridisation caused by the intrusion of felsic magma into a mafic magma chamber. The 'input' felsic magma is modelled by a cold, low density fluid and the 'resident' mafic magma by a layer of fluid wax close to its solidification point. The cold, rising input drives convection and solidification in the resident fluid, and the solidification causes significant perturbations to an otherwise simple input flow, greatly enhancing mixing and mingling between the two model magmas. The dimensionless parameters controlling the evolution of the system are determined and different morphologies of the solid mass fit into clearly defined fields in the parameter space. The most important implication of the experiments is that the freezing of mafic chambers due to felsic intrusion may give rise to intense hybridization of large volumes of magma. This potentially important mechanism for hybridization has, to date, received little attention in the literature. © 1998 Elsevier Science B.V. All rights reserved.

Keywords: felsic composition; mafic magmas; fluid dynamics; models

1. Introduction

Hybridisation of magmas through mixing and mingling has now become established as a major petrogenetic process [1]. The mixing of magmas results in a homogenous rock of intermediate composition, whereas in a mingled rock, the end-members are dispersed or intertwined in each other, typically on a centimetre to decimetre scale, but retain their compositional identities. Using fluid dynamical experiments, we investigate hybridisation caused by

the intrusion from below of low density, cold felsic magma into a mafic magma chamber.

Most past work on magma hybridisation has considered the replenishment of a felsic magma chamber by intruding mafic magmas; however, the intrusion of felsic magmas into mafic chambers may be more common than so far realised [2]. It is well known that the order of emplacement of magmas in many large batholiths is from more primitive magmas to more felsic magmas [2–4], providing the appropriate conditions for felsic intrusions into mafic chambers, and a few examples of granite intrusion into dioritic magma chambers have been described [2,5,6]. Identifying the intrusion of felsic magmas into mafic chambers in the field is difficult because: (a) the dispersion of mafic enclaves in the felsic intruder

^{*} Corresponding author. Tel.: +61 (6) 249-3242; Fax: +61 (6) 249-0738; E-mail: alison.leitch@anu.edu.au

¹ Present address: Department of Earth Sciences, Oxford University, Parks Road, Oxford OX1 3PR, UK.

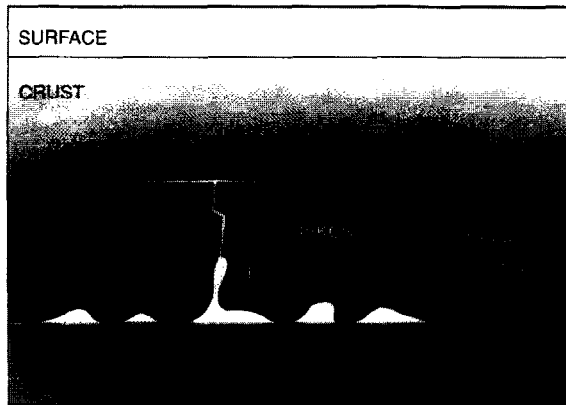


Fig. 1. Schematic cross section of the crust in an Andean-type tectonic region, showing a scenario where felsic magma may intrude a mafic magma chamber. See text.

may be mistaken for the intrusion of mafic into felsic magma; (b) granitic magma can remain liquid as it intrudes a hot mafic chamber, and may simply rise to form a stratified magma chamber [6,7]; (c) frozen mafic enclaves may sink out of the granite towards the base of the magma chamber [7]. The geological record of the passage of granite through a mafic chamber may thus be restricted to geochemical mixing trends and to the presence of mafic enclaves in the granite.

The intrusion of felsic magma from below requires the mafic magma to be emplaced above the felsic magma source. We envisage a situation in which hot (1100–1300°C) mafic magmas underplate the crust (Fig. 1). Fractionated mafic magmas feed intracrustal bodies and felsic crustal melts, then rise to intercept these bodies. The felsic magmas are significantly cooler than the mafic magmas because heat from the underplating magma is used to melt the crust rather than raise its temperature. When the melt fraction of the partially molten crust reaches 10–20% (at $\sim 850^\circ\text{C}$, the buffering temperature of biotite-dehydration melting [8]), melt may become mobile and rise before it is warmed further.

Because of their higher solidification temperatures, mafic magmas tend to solidify when intruded by a cooler felsic magma. In our experiments, we concentrate particularly on the complicating effects caused by freezing of the mafic magma as the felsic magma rises through it. We begin by reviewing relevant work, then describe our laboratory experiments

and the mingling and mixing we observed. Finally, we discuss the implications for magmatic bodies.

2. Previous work

Most experimentalists studying magma mixing and mingling have considered the replenishment of chambers by more primitive magmas (e.g. Refs. [9–15]). They found that magma hybridisation is strongly restricted by density and viscosity differences which tend to keep the two end-members separate [13], the denser primitive magma ponding under the more evolved magma. Large scale mixing may occur at a late stage, when instabilities develop due to degassing or fractionation of the mafic magma [9,13]. Mixing may also result when magmas are rapidly injected into chambers as turbulent fountains [11,14], but turbulence is unlikely to develop in systems involving viscous felsic magmas.

The only experimental work considering replenishment of a chamber by light fluid was that of Huppert et al. [12], who did not include freezing. These authors discovered ranges of physical parameters in which the rising column of light inflow varies from laminar to turbulent, and showed how mixing with the resident fluid increases with the level of inflow turbulence.

Freezing of the mafic magma when interacting with a colder magma prevents mixing for a wide range of end-member compositions, volume ratios, and temperatures [16,17]. Frost and Mahood [17] concluded that homogenous mixing is possible only when the end-members have similar composition (SiO_2 content difference less than 10%), or if the mafic fraction is greater than 50%.

Several mechanisms have been suggested to explain the origin of fine-grained mafic magma enclaves that characterise mingled bodies: the forceful injection of mafic magma into felsic chambers [17,18], simultaneous ascent through a conduit or a dyke [19,20], flotation of light vesiculated mafic magma at shallow depths [9,21], and entrainment of enclaves by convection in layered chambers [10,22]. All these mechanisms require strong velocity gradients. However, mafic enclaves may also be formed in quieter environments, such as when mafic dykes are disrupted by surrounding granite [23–25]. Very often, disruption seems to occur in situ, where flow

shearing plays a minor role [2,24]: in this case, it could result from the contraction of mafic magma that accompanies freezing [2,23].

Most experimental studies on mingling have considered simultaneous flow of magmas in volcanic conduits [19,20,26]. Weinberg [27] discusses the possibility of slow magma mingling and mixing during ascent of a diapir. Snyder and Tait [15] report on mingling during slow replenishment of magma chambers, where disruption of the dense, less viscous intruding fluid was caused by buoyancy and flow instabilities at the contact between the fluids. Fink and Griffiths [28] look at the solidification of lava flows under air and water. Their experiments also apply to the quenching of dense mafic magmas ponding in a colder magma chamber: in this case, freezing inhibits magma interaction.

To our knowledge, no previous experimental work has been carried out on the freezing of mafic magma due to cold felsic intrusion.

3. Procedure and methodology

The key properties of the resident mafic and intruding felsic magmas are that the mafic magma is close to its solidification temperature and the felsic magma is colder, lighter, more viscous and miscible.

To model the resident magma, we chose polyethylene glycol (PEG600) wax because it is transparent when melted, and has a melting temperature close to room temperature. Finding an analogue to the intruding magma was problematical. Water-based materials have an unacceptable high heat of mixing with wax [29], and hydrocarbon oils are immiscible with PEG. Glycerine and ethanol are miscible and do not have large heats of mixing, but glycerine is heavier than PEG and ethanol is much less viscous. We compromised with a 3 : 2 by volume mix of glycerine and ethanol [30]. This has a lower viscosity than PEG at the same temperature (30 cf. 180 mPa s at 20°C), but the viscosity increases strongly as temperature decreases, to about 100 mPa s at 0°C and 220 mPa s at –10°C. Our input fluid was recycled several times, and it became denser and more viscous due to evaporation of alcohol and contamination by PEG, so there was some variation of input density and viscosity in our experiments.

This input fluid rose as a smooth, laminar column. To investigate the effect of an unstable column, we used a 1 : 3 volume ratio of glycerine and ethanol. This had a viscosity of 9 mPa s at 20°C, 25 mPa s at 0°C and 40 mPa s at –10°C. Physical properties of the materials are given in Table 1.

Most experiments were performed in a perspex tank with dimensions shown in Fig. 2b. To gauge the importance of wall effects, we also carried out some experiments in a larger tank (30 × 30 × 30 cm). The tank was filled to depth h with the resident fluid, just above its solidification temperature T_m , and the cold intruding fluid was injected through a 0.6-cm-diameter hole centred in the base of the tank. The input fluid was controlled at several degrees below T_m by a refrigeration unit and heat exchanger as shown in Fig. 2a. The input flow was maintained at volume flux Q by a peristaltic pump. Q was measured before each experiment and checked by monitoring the rate at which the tank filled.

The experiments were observed using the shadowgraph technique, diffuse back lighting or front lighting from an arc lamp, and recorded on still photographs and video films. Thermistors monitored the temperature within the overlying layer of input fluid and at the discharge point (Fig. 2b). Temperatures were logged onto a computer every 2 s. Fluid samples were taken with syringes attached to hypodermic tubing and densities measured by a precision digital densimeter. Viscosity was measured with a Haake roto-viscometer.

4. System and controlling parameters

The input fluid affects the system in two basic ways: rising through the layer it drives convection and it causes solidification of the resident liquid. Thus, we expect the system evolution to be controlled by the rates of deformation and solidification. These, in turn, are determined by the buoyancy flux of the input and its temperature deficit. We also expect the viscosity ratio between input and resident fluids to play a role, since this is a key factor in the way the fluids interact.

From the variables in Table 1, we can construct dimensionless parameters which characterise the system. We neglect the buoyancy of the solid as it was usually of secondary importance, and while strength

Table 1
Physical variables

Symbol	Meaning (units)	Experiments	Magma chambers
A	surface area (m ²)	0.0075/0.09	10 ² –10 ¹⁰
c_i	specific heat input (J/kg/°C)	2270	1500
c_r	specific heat resident (J/kg/°C)	2460	1500
h	height of resident layer (m)	0.06/0.12	10–3 × 10 ³
L_r	latent heat resident (J/kg)	1.46 × 10 ⁵	3 × 10 ⁵
Q	input flow rate (m ³ /s)	0.3 – 3 × 10 ⁻⁶	10 ⁻¹ –10 ²
r	input column radius (m)	Eq. 1	
T_i	temperature input fluid (°C)	-9 to +14	700–1100
T_r	resident temperature (°C)	17.2–21.5	1050–1250
T_m	solidification temperature resident (°C)	19.5/17.5	1000–1250
ΔT_i	$T_m - T_i$ (°C)	5–28	20–550
ΔT_r	$T_r - T_m$ (°C)	0–2	0–50
T'	$(T - T_i)/(T_r - T_i)$		
η_i	viscosity of input (Pa s)	0.1–0.22	10 ³ –10 ⁸
η_r	viscosity resident (Pa s)	0.18	10–10 ⁴
η_s	solid viscosity/strength (Pa s)	?	10 ⁴ –10 ¹⁰ ?
κ	thermal diffusivity (m ² /s)	9 ± 1 × 10 ⁻⁸	5 × 10 ⁻⁷
ν	kinematic viscosity η_r/ρ_r (m ² /s)	1.6 × 10 ⁻⁴	4 × 10 ⁻³ –10
ρ_r	resident density (kg/m ³)	1126.5	2500–2700
ρ_i	input density (kg/m ³)	1087–1119	2250–2500
ρ_s	solid density (kg/m ³)	1200	2500–2900
$\Delta\rho_i$	input density deficit (kg/m ³)	8–45, 170	50–400
$\Delta\rho_s$	solid density excess (kg/m ³)	74	50–300
ρ'	$(\rho - \rho_i)/(\rho_r - \rho_i)$		

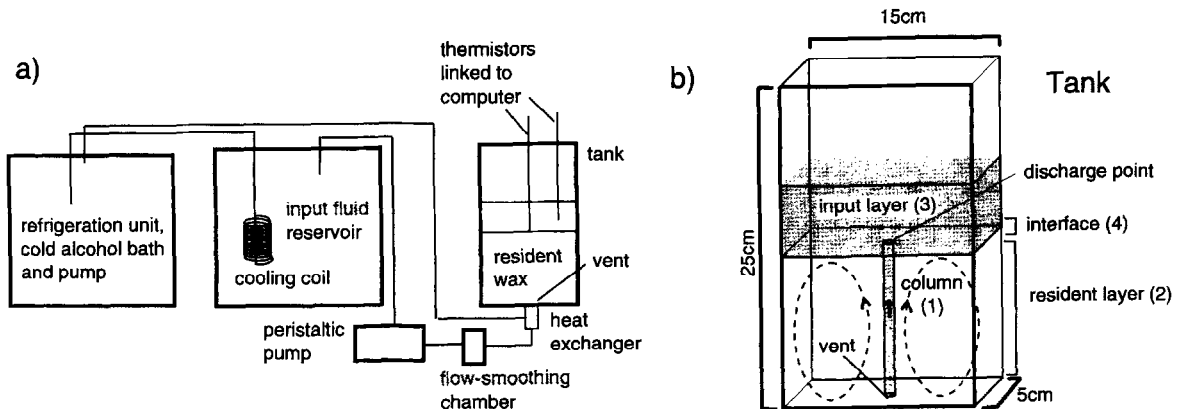


Fig. 2. (a) Experimental set up. All fluid pathways were insulated and precooled before an experiment. The temperature gain between fluid reservoir and input vent was about 10% of the difference between the reservoir and room temperature. Flow pulses caused by the action of the peristaltic pump were minimized by the presence of a flow-smoothing bubble chamber. (b) Schematic diagram of the tank. Input fluid is introduced to the bottom of the resident wax layer at the 'vent'. In the idealized case, it rises as a column and flows into an upper layer at the 'discharge point'. The horizontal contact between the upper and lower layers is referred to as the 'interface'.

and rheology of the solid are clearly important, we do not have a way to measure or control them, and, therefore, exclude them. We are left with the pa-

rameters defined in Table 2. Gr and Re relate the buoyancy and volume flux of the input, which tend to drive convection, and the viscosity of the sur-

Table 2
Dimensionless parameters

Symbol	Name	Definition	Experiments	Magma chambers
Gr	Grashof number	$g(\Delta\rho/\rho)h^3/v^2$	$5 \times 10^2 - 2 \times 10^4$	$10 - 10^{15}$
Re	Reynolds number	Q/hv	$10^{-2} - 2 \times 10^{-1}$	$10^{-8} - 1$
GrRe	Grashof–Reynolds number	$g(\Delta\rho/\rho)Qh^2/v^3$	$3 \times 10^1 - 3 \times 10^3$	$10^{-4} - 10^{12}$
Pe	Peclet number	$Q/h\kappa$	$3 \times 10^1 - 3 \times 10^2$	$10 - 10^7$
St	Stefan number	$(L + \Delta T_r c_r)\rho_r/c_i\rho_i\Delta T_i$	2.4–14.4	0.4–10
R	viscosity ratio	η_r/η_i	0.07–1	0.1– 10^7
D_s	solid density ratio	$\Delta\rho_s/\rho_r$	0.07	0.02–0.12

roundings which tends to hamper it. Pe compares the advection of matter with the diffusion of heat; St relates the heat deficit of the input to the latent and specific heat capacity of the resident fluid, and R is the viscosity ratio of the input and resident fluids.

The radius, r , of the input column can be found from a dimensional analysis of a laminar column rising through a layer of indefinite lateral extent. We can balance the workrates of the buoyancy and viscous forces, $W_b = (\Delta\rho g\pi r^2 h)w$ and $W_\mu \sim \tau h^2 w$. Assuming the column drives a convection cell of size h , the shear stress is $\tau \sim \mu_r w/h$. Remembering that the average velocity in the column $w = Q/\pi r^2$, we obtain

$$r \sim h (\text{Re}/\text{Gr})^{1/4} \quad (1)$$

and the time for the column to rise through the layer

$$t_h \sim t_v (\text{GrRe})^{-1/2}$$

where t_v is the viscous diffusion timescale h^2/ν . A smaller t_h/t_v implies a larger deformation rate for the resident fluid, thus GrRe is a reasonable measure of the importance of the buoyancy flux in deforming the layer. A corresponding measure of the importance of solidification is the thickness of solid produced along the wall of the rising column in time t_h , relative to the radius of the column. If we assume that all the heat deficit of the input is used to create solid, it is given by the Stefan number, St.

5. Results

Table 3 is a list of experiments, including values of key input variables and the controlling parameters defined above. In calculating R , the viscosity of the input fluid is taken at a temperature intermediate

between those of the vent and the resident fluid. Our principal results consist of observations of the flow patterns and growth patterns of solidifying wax as functions of GrRe and St, as summarized in Fig. 3. The four areas are mainly controlled by St, but there are significant differences in each as GrRe changes. The uncertainties in St are about 15% due to uncertainties in T_i and T_m , and therefore the regime boundaries are only approximate.

We describe below six illustrative experiments (Fig. 4), starting with four experiments at low buoyancy flux and increasingly cold inflow.

5.1. Low buoyancy flux (GrRe < \sim 1000)

5.1.1. Convecting cell (St > 8–8.5)

The experiments with warmest input produced a relatively simple convection pattern which evolved due to the negative buoyancy of the solidifying wax. Initially, there was no solidification and a smooth column of input fluid rose through the layer (Fig. 4a1) driving a toroidal convection cell with a width comparable to the layer depth h . Solidification did not occur along the column because the outer parts of the column were quickly warmed above T_m by contact with the wax. On discharge into the upper layer, the coldest and therefore heaviest, central fluid from the column flowed out slowly along the interface and over time caused some solidification in the form of small flat pieces in the underlying wax.

The dense solid pieces with some attached input fluid sank, and a compromise convection cell resulted, somewhat narrower than h and outlined by a cloud of solid wax particles (Fig. 4a2). Rising solid lumps sometimes disturbed the input column and enhanced fluid mixing (Fig. 4a2). Some entrained input fluid later rose as secondary plumes (Fig. 4a3).

Table 3
Summary of experiments

Experiment	Q	$\Delta\rho_i$	h	T_m	T_i	GrRe	St	Pe	R
P1	0.72	40	0.12	19.5	-8.7	650	2.4	67	0.73
P2	0.72	35	0.12	19.5	5.7	570	4.9	67	0.49
P3	1.6	30	0.12	19.5	5.5	1100	4.9	150	0.52
P4	1.3	20	0.12	19.5	-6.0	580	2.6	120	0.89
P5 ^a	1.5	20	0.12	19.5	(9.9)	690	(7.0)	140	0.52
P6 ^a	1.6	24	0.12	19.5	(13.7)	830	(11.7)	140	0.43
P7	2.9	20	0.12	19.5	13.8	1300	11.8	270	0.46
P8	3.1	39	0.12	19.5	5.0	2680	4.7	280	0.48
P9	2.3	36	0.12	17.5	-1.7	1830	3.5	210	0.66
P10	2.5	27	0.12	17.5	-7.1	1530	2.7	230	0.90
P11	0.30	37	0.12	17.5	6.6	250	6.2	28	0.50
P12	0.30	28	0.12	17.5	7.0	190	6.4	28	0.55
P13	0.34	32	0.12	17.5	12.3	240	12.8	31	0.45
P14	0.33	28	0.12	17.5	9.1	210	8.1	31	0.51
P15	0.33	16	0.12	17.5	-7.8	120	2.7	30	1.04
P16	0.67	41	0.12	17.5	11.1	610	10.5	62	0.42
P17	0.38	35	0.12	17.5	8.7	290	7.6	35	0.48
P18	0.64	27	0.12	17.5	8.1	390	7.0	59	0.57
P19	0.31	17	0.12	17.5	-0.9	120	3.6	29	0.87
P20	0.64	15	0.06	17.5	4.9	54	5.3	120	0.73
P21	0.64	11	0.06	17.5	10.4	40	9.3	120	0.66
P22	0.65	8	0.06	17.5	12.9	29	14.4	120	0.62
P23	0.57	8	0.06	17.5	0.1	26	3.7	110	1.01
P24	0.64	29	0.06	17.5	0.4	104	3.9	120	0.70
P25	0.63	181	0.12	17.5	-9.6	2550	2.9	58	0.08
P26	0.65	170	0.12	17.5	0.3	2480	4.4	60	0.08
P27	0.64	171	0.12	17.5	8.9	2450	8.9	59	0.06
P28	0.66	164	0.12	17.5	4.5	2430	5.9	61	0.07
PH1	1.2	41	0.12	17.5	-8.7	1120	2.7	110	0.73
PH2	1.45	43	0.12	17.5	2.7	1410	4.8	130	0.46
PH3	1.45	45	0.12	17.5	5.7	1450	5.8	130	0.45

Units: Q (10^{-6} m³/s), $\Delta\rho_i$ (kg/m³), h (m), T_m and T_i (°C).

^a St anomalously high (~ 15%) for observed solid morphology.

As the amount of solid wax increased, it changed the pattern of convection. The first effect was a gradual decrease in cell size (Fig. 4a2, a3). The second was a developing asymmetry. Larger amounts of solid wax sinking on the left side of the tank enhanced the convective velocities. The column then leaned over, preferentially feeding cold fluid onto the interface to the left and further enhancing solidification. A strong, narrow cell developed to the left of the column, while on the right there was a wide, diffuse cell with little solid wax (Fig. 4a3).

5.1.2. Cone ($6 < St < 9$)

For a cooler input, the top part of the column acquired a thin veneer of solid wax, which folded

and crumpled as the fluid discharged into the upper layer. The dark, crinkled outline of the column at mid depths in Fig. 4b1 is the wax veneer. At first, the folded wax was expelled with its contents at the interface forming a mingled layer. Later, it accumulated in a loosely packed cone which grew down towards the input vent (Fig. 4b2).

As the cone grew, input fluid flowed in irregular sheets around the outside of the cone, mixing with and cooling the fluid wax. It flowed out beneath the mingled layer at the interface. Eventually, the input column was encapsulated in a solid wax carapace (Fig. 4b3). The textured nature of the upper layer in the shadowgraph (cf. Fig. 4a3) indicates fine scale density variations. The cloudy region in the centre

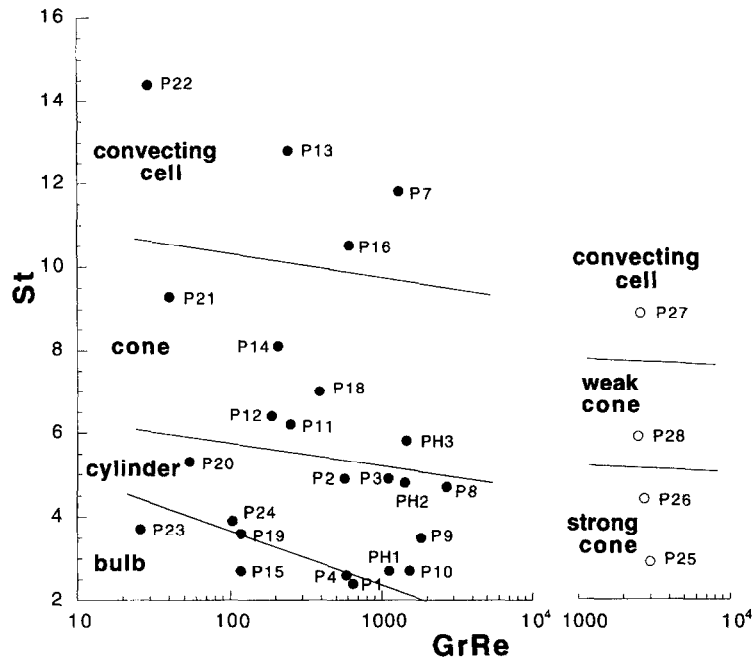


Fig. 3. Solid wax morphology observed in the experiments in the parameter space St versus $GrRe$. Experiment numbers given next to points. Open symbols on the right for experiments with low input viscosity. P5 and P6 (not shown) were anomalous due, we judge, to inaccuracies in the measurement of T_i .

of the upper layer is the input fluid discharging from its many pathways through the permeable solid structure. It rises up through a thick layer of denser, contaminated input fluid and then flows sideways.

Once solid wax encapsulated most of the input flow, for this and colder experiments, thermal buoyancy drove downflow in the resident layer on the outside of the encapsulated column.

5.1.3. Cylinder ($St < \sim 5$)

For a still colder input, a vertical pipe of solid formed around the input column before it reached the top of the layer. The pipe then tilted and ruptured near the top and base where the walls were thinnest (Fig. 4c1) giving rise to a number of small plumes. These small extrusions were encapsulated in their turn (Fig. 4c2). The solidified region thickened, producing a column of solid wax permeated by irregular tubes and sheets of input fluid (Fig. 4c3).

5.1.4. Bulb ($St \leq 3$)

With very cold input and low buoyancy flux, a thick carapace of solid wax formed around the input column before it had risen far from the vent.

Fractures near its thinnest regions allowed input fluid to escape and rise up in sheets on the outside, building another layer of solid in a structure like an onion bulb (Fig. 4d1). In Fig. 4d1, the fluid rising in narrow plumes from the top of the bulb had lost most of its heat deficit and so generated only small slivers of solid on its way to the top of the layer. Because of its long contact time with the resident fluid, the first fluid into the upper layer was relatively warm and contaminated with wax, and its presence hindered solidification at the interface. At a later time, solidification occurred in irregular upright sheets between the vent and the interface (Fig. 4d2). Still later, small wax slivers carried to the interface at early times dissolved into the mixed interface region (cf. Fig. 4d2, d3). Note that here and in Fig. 4f, we see a cross section of the wax structure where it intersects the tank walls.

5.2. Large buoyancy flux ($GrRe > \sim 1000$)

5.2.1. Convecting cell

Experiment P7 (Fig. 4e) was similar to P13 (Fig. 4a), but had a much higher buoyancy flux.

Cold material was introduced 8.5 times faster in P7, so that Fig. 4a3 should be compared with a snapshot intermediate between Fig. 4e1 and e2. Faster flow (higher Pe) in P7 also means that heat transfer efficiency between column and resident fluid is lower than for P13, so that there is a greater tendency in P7 for the input to cool and solidify the resident layer from above. A thicker, more cohesive solid layer formed on the interface and it was swept into the convection cell further from the discharge point (Fig. 4e1). The negative buoyancy of the solid had a smaller influence on the more vigorously convecting cell, which was also able to carry pieces of solid wax into the upper layer. Larger pieces of solid within the resident fluid disrupted the column, and partially blocked the discharge point. In Fig. 4e2, a tongue of input fluid is emplacing to the left below the dark solid layer. Such outflows eventually generated a series of layers of solid and glycerine (Fig. 4e3).

5.2.2. Cylinder

Experiment P10 (Fig. 4f) had a higher input buoyancy flux than P19 (Fig. 4c). The development of the solid was similar to P19, but the solid structure was more disrupted, and small pieces of solid wax (dark specks near top of figure) were carried into the upper layer by the more vigorous flow. Compare the position of the top of the solid in Fig. 4f and 4c3: because the solid encasing the input flow was broken more at higher $GrRe$, the 'hold-up' of input fluid within the solid structure is much greater.

5.3. Large tank experiments

Experiments in the narrow tank (Fig. 2b) were economical in fluids, easy to regulate, and allowed good visualization. However, the closeness of the front and back walls meant that the walls intersected the convection cell in the resident layer and the solid structure at long times, and may have hindered the sinking of solid structures. We carried out three

experiments (PH1–PH3) in a larger tank and found that patterns of convection and solidification were qualitatively the same at similar values of St and $GrRe$, and that solidified wax at the interface or around the input column did not sink even when it was not attached to the tank boundaries. Solid at the interface grew as a shallow dish. This and the attached cone floated like a boat on the resident layer.

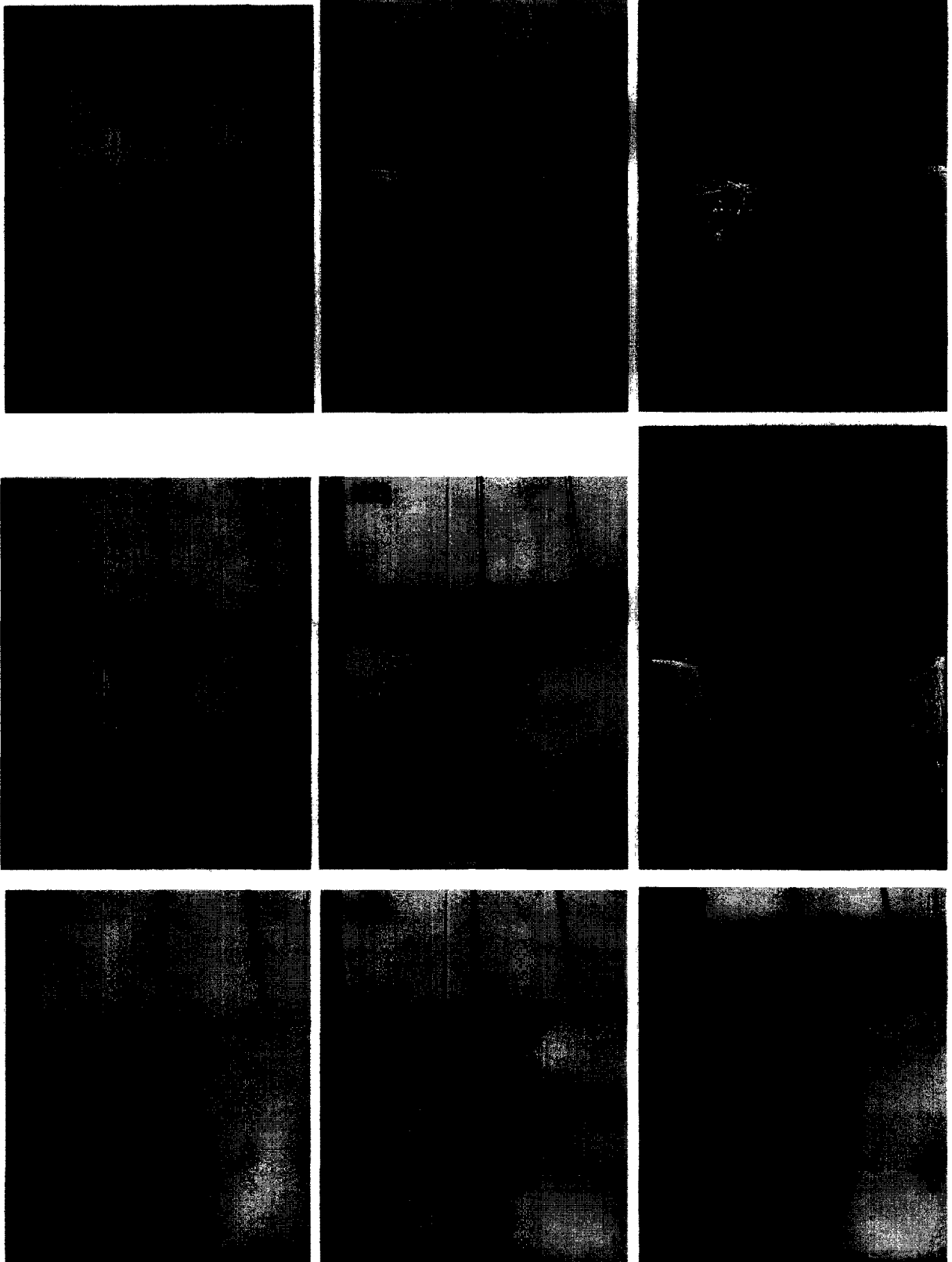
In the larger tank, the input fluid discharged over a much larger surface area, therefore the upper layer was much thinner, there was more contact between the layers and more solidification at the interface.

5.4. Low viscosity ratio experiments

For the experiments above, in the absence of solidification effects, the input always occurred as a laminar column: parameters Re_i and Re_e of Huppert et al. [12] were between 0.5 and 4.5, in their laminar flow regime. Since increasing the buoyancy flux further was difficult, we generated an unstable column by reducing the viscosity of the input. Experiments P25–P28 had $R \sim 0.07$, $Re_e \sim 1.2$ and $Re_i \sim 14$, and were in the region for varicose instability of the column [12] (see Fig. 5). The column instability led to an increased contact area and some mechanical mixing between input and resident fluids, so that a thick mixed region formed at the interface. Solid formed in thin flakes and tubes around the column, further disrupting the flow. 'Cone' structures built from the solid pieces were loosely packed and porous. For the warmest input, many tiny solid pieces were carried into the upper layer, forming an inverted cone (Fig. 5), and then tumbled back towards the interface, where some dissolved and some entrained into the lower layer.

The results in Fig. 3 (right) show some continuity with results at higher R ; however, R is clearly an important parameter in defining solid morphology.

Fig. 4. Snapshots at three different times (time in seconds at lower left) from six selected experiments (experiment number on first snapshot of each series), showing the markedly different solid structures that result as St and $GrRe$ are varied. (a–d) Increasingly cold input fluids at low input buoyancy flux. (e–f) Warm and cold input fluids at higher buoyancy flux. (a) P13, $St = 12.8$, $GrRe = 242$: a1, back lighting; a2, a3, shadowgraph. (b) P14, $St = 8.1$, $GrRe = 207$: b1, backlighting; b2, front lighting; b3, shadowgraph. (c) P19, $St = 3.6$, $GrRe = 118$, front lighting. (d) P15, $St = 2.7$, $GrRe = 117$, front lighting. (e) P7, $St = 11.8$, $GrRe = 1300$: e1, e2, back lighting; e3, front lighting. (f) P10, $St = 2.7$, $GrRe = 1525$, front lighting.



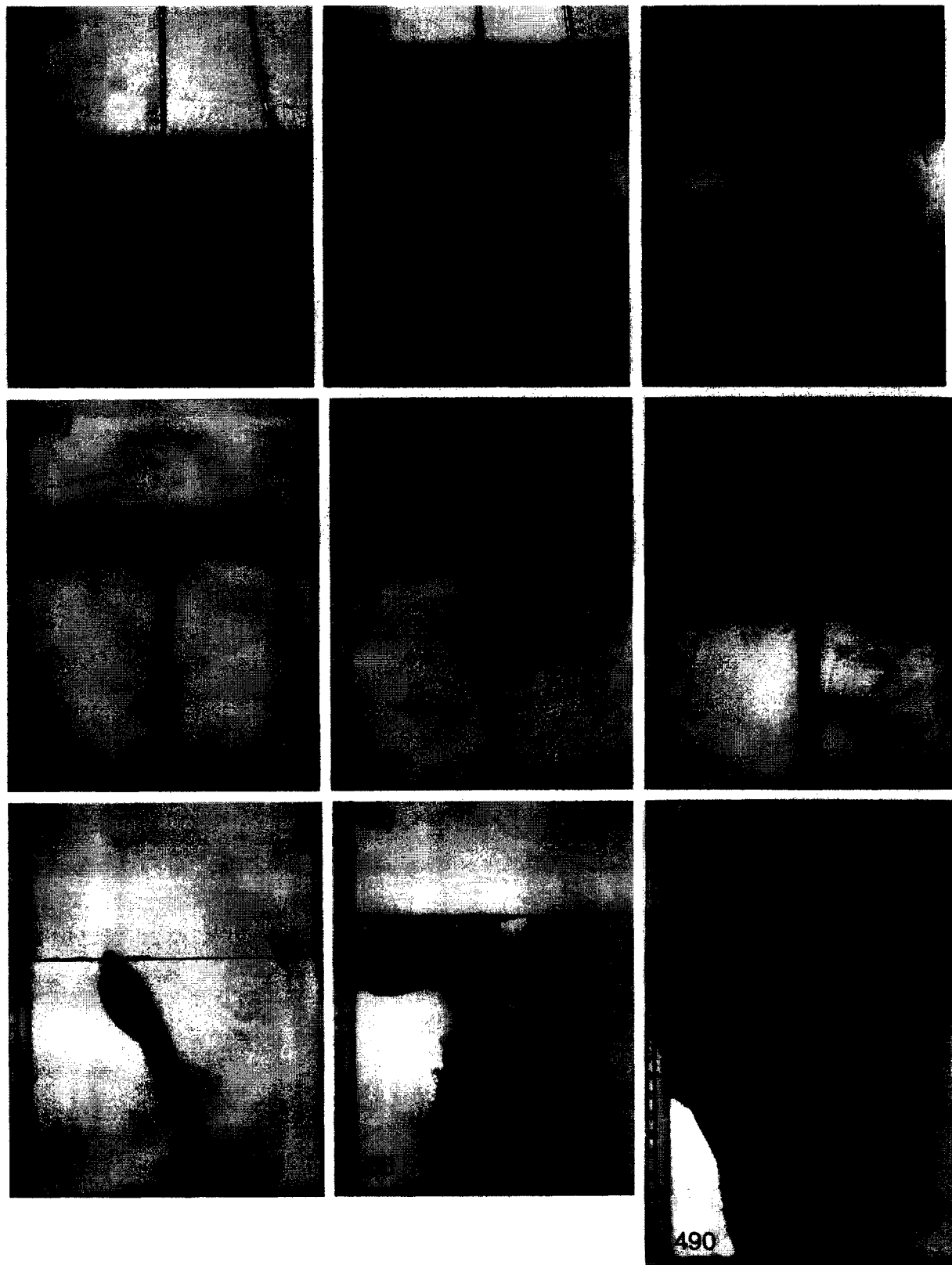


Fig. 4 (continued).

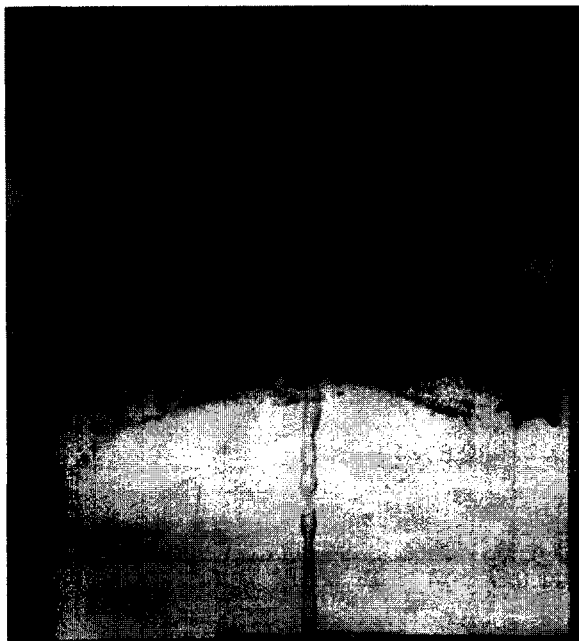


Fig. 5. Column instabilities and solidification pattern for a low viscosity input fluid. P27, $St = 8.9$, $GrRe = 2450$, $R = 0.06$, back lighting.

5.5. Evolution and structure of the upper layer

The efficiency of heat transfer between the input and resident fluids, and the degree of compositional contamination of the upper layer by resident fluid, are measures of the intensity of interaction of the fluids. To see how fluid interaction varied with the degree of solidification, in Figs. 6–8 we look at heat transfer and contamination for experiments P12–P15, which have similar values of $GrRe$, but varying St .

Fig. 6 shows how the temperature of the input fluid at the discharge point (Fig. 2b) varied with time. Results are presented in terms of normalized temperature T' versus dimensionless time $t' = t/t_h$. T' (Table 1) is the ratio between the temperature gain by the input fluid from the resident fluid to the maximum possible gain, and so is a measure of heat transfer efficiency. We assume that the measured temperature was representative of the discharge.

An approximate theoretical temperature profile across the column can be found from a simple one-dimensional analysis. Because of the similar viscosities of input and resident fluid, there was little

difference ($< 20\%$) between the velocity at the centre of the column and that at the edge. Therefore, as a disc of fluid moves from the vent to the discharge point, its temperature changes simply due to radial conduction of heat. We assumed that at the vent $T = T_i$ within the column and $T = T_r$ outside, and used equation 7.6(4) of Carslaw and Jaeger [31] to find the temperature distribution at time t_h . This depends only on Pe , which was very similar for P12–P15. For $Pe \sim 30$ the analysis predicts T' is 0.1 at the centre of the column, 0.6 at the edge and 0.35 on average. The average is drawn as a horizontal line in Fig. 6.

The only experiment in which the input resembled a simple column, P13, showed wide variations in the discharge temperature on a short time scale, but a nearly constant long term temperature. The average was a little higher than the theoretical value, that is, heat transfer was higher than expected. It may have been enhanced due to stirring by solid wax pieces, or the theoretical value may be inaccurate due to error in the value of κ for the experimental fluids. Significantly, the range of temperatures observed 0.1–0.6 is similar to that predicted by the simple model.

For the other (colder) experiments, a cone or bulb grew around the input column. At the early stages, the heat transfer was increasingly efficient for increasingly cold input, due to the greater contact between input and resident fluids as the input column broke up into numerous narrow plumes (Fig. 4d). Later, T' decreased in all cases as growing solid wax insulated the input fluid. Eventually, heat transfer was less efficient than the ideal case.

Note that the two cone cases, P12 and P14, show a reversal of the general trend: the colder input produced less efficient heat transfer. This shows the sensitivity of heat transfer to random perturbations. In P14, the growing cone collapsed sideways at an early stage building a broader-based structure and causing the input column to spread and mix more.

Fig. 7 and 8 show profiles of normalized temperature T' and density ρ' (at 20°C) in the upper input fluid layer for experiments P12–P15. ρ' (Table 1) is a measure of the compositional contamination of the input fluid. Density profiles were taken at the end of the experiments, whereas temperature profiles were taken during the experiments: the height h' for

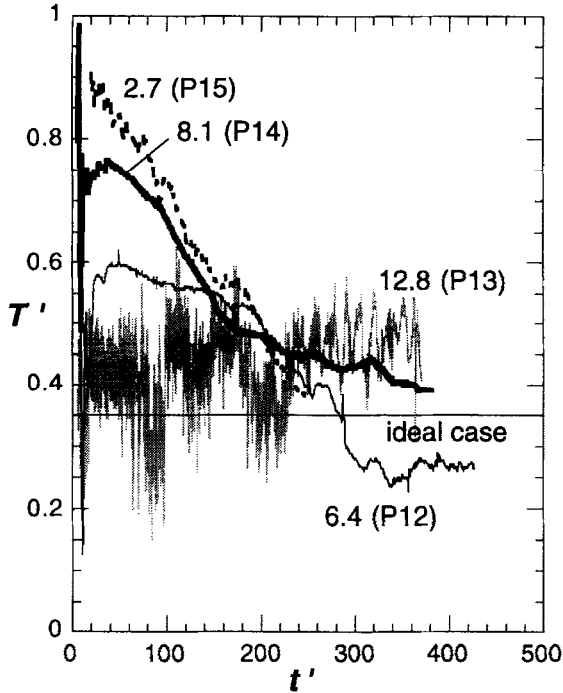


Fig. 6. Dimensionless temperature T' at the discharge point versus normalized time $t' = t/t_h$ for a series of experiments with similar buoyancy flux, but differing input temperatures. Curves are labelled with value for St and experiment number (in brackets). Line at $T' = 0.35$ corresponds to theoretical average for an ideal case.

each temperature measurement was normalized by the height of the upper layer at the measurement time.

Both Figs. 7 and 8 show that heat transfer and mixing are greatest for the coldest input ($St = 2.7$) and least for the warmest input ($St = 12.8$). As also suggested by Fig. 6, heat and mass transfer are enhanced when solidification disrupts the flow and increases the contact between the input and resident fluids.

The temperature profiles in Fig. 7 show an inversion, usually associated with a sharp turning point. The inversion point marks the top of a compositionally mixed region, and where discharge of the input fluid was strongest. This fast-flowing cold region can be seen as a horizontal shadowed region in the upper layer in the shadowgraph Fig. 4b3. Below this point, temperature increased downward due to increased mixing with warmer resident fluid. Above it, temperature increased upward due to heat leakage

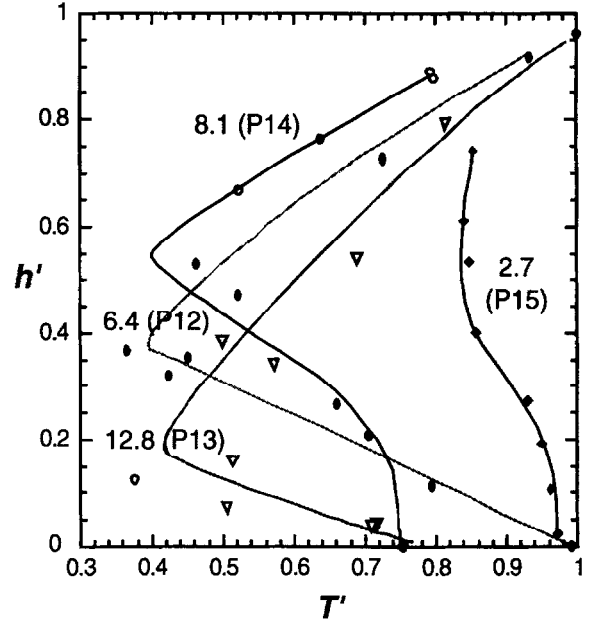


Fig. 7. Dimensionless temperature T' versus normalized height h' within the upper layer (Region 3). $h' = (y - h_{int}) / (h_{top} - h_{int})$. Initially, input fluid/resident fluid interface is at $h' = 0$. Labels as in Fig. 6.

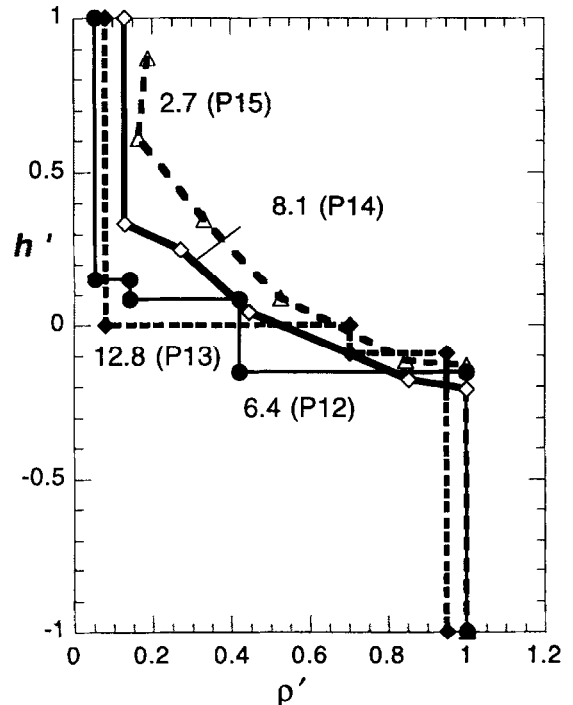


Fig. 8. Dimensionless density $\rho' = (\rho - \rho_i) / (\rho_r - \rho_i)$ as a function of h' . Labels as in Fig. 6.

from the laboratory and because fluid discharged at earlier times was warmer (Fig. 6). For the warmest input ($St = 12.8$), the inversion point is close to the interface, indicating that the compositionally mixed layer is thin. For the other cases inversion occurs near the centre of the layer suggesting that a large fraction of the input fluid was contaminated.

All of the curves in Fig. 8 show some degree of contamination of the input fluid by the resident fluid. Only the 'convecting cell' case shows contamination of the resident liquid: this occurred as fluid from the interface was dragged down with solid wax pieces.

5.6. End stages

The evolution of the system after we turned off the input flux depended on the morphology of the solid. If the input column was completely encapsulated, we observed melting and dissolution of the solid on a timescale of hours. For cones which were not totally encapsulated, input fluid within the solid slowly drained into the upper layer. For experiments in the convecting cell regime, without the dynamic support of the rising input fluid, the dense solid slowly sank, carrying trapped input fluid with it. The trapped fluid was slowly released and mixed as it rose. For a low viscosity input, the solid pieces were smaller and surrounded with lower viscosity fluid, and so the solid-rich layer sank quickly leaving a broad zone of mixed fluid.

5.7. Overview

Our experimental system may be divided into the four areas of Fig. 2b, with different mixing and mingling processes occurring in each. In region 1, the input column rose, causing solidification which, in turn, disturbed the column on mm to cm scales. The physical barrier of the solid hindered mixing by chemical diffusion, but the multiscale perturbation of the laminar flow led to physical mingling and mixing of the fluids. When the column itself was unstable (in the absence of solidification), its fluctuations led to increased mixing and mingling. We observed a systematic change in solid structure reflecting where solidification first occurred: at the interface, producing pieces circulating within the wax layer; near the top of the column, leading to a crumpled cone

growing downwards; or near the vent, producing an intricate maze of vertical sheets and tubes.

Fluids and solid particles from region 1 fed into the upper layer, region 3. The nature of fluid discharged into region 3 changed with time, generally becoming colder and less contaminated as the input became thermally and chemically insulated from the resident fluid by encapsulating solid. Denser, warmer mixed fluids spread at the interface, while less contaminated input fluid was expelled higher in the layer.

Region 2 (the resident layer) convected upwards in the centre due to viscous coupling with the rising input fluid. If the column became encapsulated, thermal buoyancy drove convection down at the centre. Solid pieces originating at the interface might sink and modify the convection, and particularly when a mixed layer existed at the interface, input fluid might be dragged into the resident layer attached to these solid pieces. Plumes of incompletely mixed input fluid might then rise slowly back to the interface.

Region 4, the interface, was nearly always characterized by a mixed layer which originated mainly from mixing during the rise of the input fluid in region 1 and from the dissolution of solid carried into the upper layer. This last effect was observed in all experiments and became increasingly important the longer the experiment progressed. Particularly for the tank with the large surface area, solidification of the resident fluid from above was an important process. In relatively wide, shallow systems we might expect it to be the dominant process, especially once region 1 is encapsulated by solid.

6. Discussion

In relating our results to magmatic systems, we must identify the range of values taken by the controlling dimensionless numbers in natural systems, and also consider the influence of additional factors not modelled in our experimental system. Complexities in geometry, rheology and flow history fall into this latter category.

In Table 1, we have assembled representative ranges for the physical variables in magmatic systems. The most uncertain of these is the input flow rate, Q . Rates between 10^{-4} and $1 \text{ km}^3/\text{yr}$ (3×10^{-3} –

30 m³/s) are probably reasonable in the long term (tens to thousands of years), but may not reflect typical conditions of a single inflow event (F. Spera, personal communication). Assuming that the felsic magma rises from its source region in a dyke, and that dykes pinch off into columns which focus flow from between 3 and 30 dyke widths, from the analysis of Petford et al. [32] we find flow Q for a magma pulse in the range 10^{-1} – 10^2 m³/s.

Due to the variability in h , η and Q in natural systems, the values of GrRe, St and R in Table 2 span a vast range, extending far beyond that of our experiments. To match the values of R in our experiments, the viscosities of input and resident magmas would be 10^3 – 10^4 Pa s. To match GrRe, we require very high Q into a small system ($h \sim 10$ m) or very low Q into a large system ($h \sim 1000$ m).

6.1. Magma properties

In nature, the viscosity of felsic magmas is usually larger than that of basic magmas. However, in our experiments, the viscosity ratio R of input to resident fluids was around unity or much less. The viscosity ratio is important in determining the type of instabilities which form at the interface of two fluids which, in turn, has a bearing on the mixing [12]. Therefore, as far as mixing is concerned, R is not important when the inflow is laminar, as it was in the beginning of most of our experiments, or when fluid–fluid contact is prevented, as it was at later times when frozen wax encased the input. We reduced R in experiments P24–P28 to investigate the effect of column instabilities (which might occur at higher buoyancy flux) on solidification and mixing.

An important difference between experiments and nature is that PEG wax solidifies over a small temperature range (0.5–1°C), whereas magmas crystallize over a range of 100°C or more. As the melt fraction in magmas decreases, they become increasingly viscous, until a critical melt fraction (CMF, [33]) is reached, generally at 30–45% melt, where viscosity increases sharply. For melt fractions below the CMF, the magma will behave essentially as a solid. Thus, for natural systems, it may be appropriate to consider the solidification temperature to be the temperature at the CMF and to use a reduced value of latent heat. If cooling were fast enough,

the solid created could be a glass and very little latent heat would be involved. However, crystallization rates are so fast in mafic magmas [34] that this is very unlikely to happen.

An important parameter that we have been unable to explore is the strength of the solid relative to the pressure of the intruding magma. This has bearing on how readily the inflow can break the solid structure. For a weak solid, such structures as cylinders and bulbs would be disrupted before they could properly form. A solid strength parameter will generate another dimension in our parameter field of Fig. 3.

6.2. Magma chambers

Magma chambers occur in a variety of shapes and sizes, some rather dissimilar to our experimental tank. The main region of fluid interaction is between the vent and discharge point over the scale of the resident layer depth, h . This scale also controls the size of the convection cell in the resident fluid and the size of the main region of mixing. Therefore, we would expect most hybridisation, as a percentage of the total volume, when the magma chamber is not too wide compared to its depth. We do not expect the horizontal dimensions of flat magma chambers to have direct importance in the formation of mingled structures; however, they will have bearing on whether mingled structures survive. In the experiments of Huppert et al. [12], mixing of the resident fluid continues as long as the input lasts. By contrast, in our cold experiments, fluid interaction is limited by encapsulation of the input fluid, and the encapsulation time rather than the inflow time, controls the extent of mixing.

6.3. Preservation of mingling and mixing structures

If the mingling and mixing structures formed during the experiments were to be found in the geological record they would provide important constraints on the physical conditions during intrusion of the felsic magma. Since it is difficult to unmix magmas, we would expect to find evidence of mixing, perhaps overprinted by subsequent processes. Mingled structures are harder to preserve. When one or both mingled components are liquid, it is always possible to unmix them before they solidify and are pre-

served as rocks. Observations of the late stages of our experiments show several ways in which this can occur once input has ceased.

First, the input fluid trapped within the solid will slowly escape upwards and join the overlying layer. Second, the solid mass may be partly or totally reabsorbed by the warmer surrounding liquid. If the chamber was much wider than the layer depth, then there may be heat available to completely remelt the newly formed solid. Depending on how this occurred, the remelted resident fluid could disengage from the trapped input with minimal interaction, and the result may then be a mixed region only. Third, the solid mass may become unstable and fall to the bottom of the chamber. Fourth, in nature, the solid mass may contain up to 40% interstitial melt, which may crystallize slowly after the replenishment process is over and erase evidence of its initial rapid cooling. Thus, evidence of the intrusion of felsic magma into a mafic chamber may only be the presence of hybrid rocks defining a typical mixing geochemical trend, associated with the presence of mafic enclaves in the felsic end-members. These features are ambiguous inasmuch as they could result from a variety of different igneous processes.

7. Conclusions

We carried out experiments simulating the intrusion of cold, low density felsic magma into a mafic magma chamber, and found that solidification of the model mafic magma introduced perturbations on many scales to an otherwise monotonous rising column of model felsic magma, considerably enhancing magma hybridisation (mingling and mixing). Different degrees and styles of mixing and mingling were identified based on the controlling dimensionless parameters St , $GrRe$ and R , which measure the undercooling, buoyancy flux and viscosity ratio of the input.

The experiments could be divided into four groups based on the morphology of the solid mass which grew around the input column. As the input became colder, the solid wax developed from circulating pieces within a convection cell, to a crumpled cone growing down from the discharge point, to a cylinder around the input column, to an onion-bulb

above the vent. These transformations were based on how much solidification could take place in the time the input fluid crossed the layer, which was controlled mainly by the Stefan number, St . Generally, colder inputs resulted in more hybridization because a greater amount of solidification caused more intense disruption of the inflow. As the dimensionless buoyancy flux $GrRe$ increased, the input drove more vigorous convection and was better able to break the solid structure. For a lower viscosity ratio R , the input column became unstable and small solid fragments formed within contortions of the column.

Natural geological systems cover a parameter range much greater than that of the experiments and they include processes such as the formation of individual crystals within a liquidus–solidus interval that we were unable to model in our experiments. Thus our experiments may reveal only a subset of a wealth of mixing processes which occur when felsic and mafic magmas interact in this geometry.

Acknowledgements

We would like to thank Ross Kerr and Ross Griffiths for enlightening discussions on magmatic processes, Frank Spera and Kathy Cashman for advice on magmatic flow and crystallization rates, and Stewart Turner for recommendations on dealing with anomalies. We also thank Natalie Thomas for help with the experiments, and Tony Beasley and Derek Corrigan for their excellent technical assistance. [RO]

References

- [1] R. Bateman, The interplay between crystallization, replenishment and hybridization in large felsic magma chambers, *Earth-Sci. Rev.* 39 (1995) 91–106.
- [2] R.F. Weinberg, The disruption of a diorite magma pool by intruding granite: the Sobu body, Ladakh Batholith, Indian Himalayas, *J. Geol.* 105 (1997) 87–98.
- [3] P.C. Bateman, A summary of critical relations in the central part of the Sierra Nevada batholith, California, U.S.A., *Geol. Soc. Am. Mem.* 159 (1983) 241–254.
- [4] W.S. Pitcher, M.P. Atherton, E.J. Cobbing, R.D. Beckinsale, *Magmatism at a Plate Edge – The Peruvian Andes*, Blackie and Sons, London, 1985.
- [5] R.A. Wiebe, T. Wild, Fractional crystallization and

- magma mixing in the Tegalak layered intrusion, the Nain anorthosite complex, Labrador, *Contrib. Mineral. Petrol.* 84 (1983) 327–344.
- [6] R.A. Wiebe, Rupture and inflation of a basic magma chamber by silicic liquid, *Nature* 326 (1987) 69–71.
- [7] R. Wiebe, Comingling of contrasted magmas and generation of mafic enclaves in granitic rocks, in: J. Didier, B. Barbarin (Ed.), *Enclaves and Granite Petrology*, Vol. 13, Elsevier, Amsterdam, 1991, pp. 393–402.
- [8] D. Vielzeuf, J.R. Holloway, Experimental determination of the fluid-absent melting relations in the pelitic system, *Contrib. Mineral. Petrol.* 98 (1988) 257–276.
- [9] H.E. Huppert, R.S.J. Sparks, J.S. Turner, Effects of volatiles on mixing in calc-alkaline magma systems, *Nature* 297 (1982) 554–557.
- [10] H.E. Huppert, R.S.J. Sparks, J.S. Turner, Some effects of viscosity on the dynamics of replenished magma chambers, *J. Geophys. Res.* 89 (1984) 6857–6877.
- [11] I.H. Campbell, J.S. Turner, Turbulent mixing between fluids with different viscosities, *Nature* 313 (1985) 39–42.
- [12] H.E. Huppert, R.S.J. Sparks, J.A. Whitehead, M.A. Hallworth, Replenishment of magma chambers by light inputs, *J. Geophys. Res.* 91 (1986) 6113–6122.
- [13] I.H. Campbell, J.S. Turner, A laboratory investigation of assimilation at the top of a basaltic magma chamber, *J. Geol.* 95 (1987) 155–172.
- [14] I.H. Campbell, J.S. Turner, Fountains in magma chambers, *J. Petrol.* 30 (1989) 885–923.
- [15] D. Snyder, S. Tait, Replenishment of magma chambers: comparison of fluid–mechanic experiments with field relations, *Contrib. Mineral. Petrol.* 122 (1995) 230–240.
- [16] R.S.J. Sparks, L.A. Marshall, Thermal and mechanical constraints on mixing between mafic and silicic magmas, *J. Volcanol. Geotherm. Res.* 29 (1986) 99–124.
- [17] T.P. Frost, G.A. Mahood, Field, chemical, and physical constraints on mafic–felsic magma interaction in the Lamarck Granodiorite, Sierra Nevada, California, *Geol. Soc. Am. Bull.* 99 (1987) 272–291.
- [18] R.I. Hill, San Jacinto Intrusive Complex 1. Geology and mineral chemistry, and a model for intermittent recharge of tonalitic magma chambers, *J. Geophys. Res.* 93 (1988) 10325–10348.
- [19] S. Blake, I.H. Campbell, The dynamics of magma-mixing during flow in volcanic conduits, *Contrib. Mineral. Petrol.* 94 (1986) 72–81.
- [20] A. Freundt, S.R. Tait, The entrainment of high-viscosity magma into low-viscosity magma in eruption conduit, *Bull. Volcanol.* 48 (1986) 325–339.
- [21] J.C. Eichelberger, Vesiculation of a mafic magma during replenishment of silicic magma reservoirs, *Nature* 288 (1980) 450–466.
- [22] H.E. Huppert, R.S.J. Sparks, The generation of granitic melts by intrusion of basalt into continental crust, *J. Petrol.* 29 (1988) 599–624.
- [23] R. Wiebe, Relations between coexisting basaltic and granitic magmas in a composite dike, *Am. J. Sci.* 273 (1973) 130–151.
- [24] T. Furman, F.J. Spera, Co-mingling of acid and basic magma with implications for the origin of mafic I-type xenoliths: field and petrochemical relations of an unusual dike complex at Eagle Lake, Sequoia National Park, California, USA, *J. Volcanol. Geoth. Res.* 24 (1985) 151–178.
- [25] C.G. Barnes, C.M. Allen, J.B. Saleeby, Open- and closed-system characteristics of a tilted plutonic system, Klamath Mountains, California, *J. Geophys. Res.* 91 (1986) 6073–6090.
- [26] T. Koyaguchi, Magma mixing in a conduit, *J. Volcanol. Geoth. Res.* 25 (1985) 365–369.
- [27] R.F. Weinberg, Internal circulation in a buoyant two-fluid Newtonian sphere: implications for composed magmatic diapirs, *Earth Planet. Sci. Lett.* 110 (1992) 77–94.
- [28] J.H. Fink, R.W. Griffiths, Radial spreading of viscous-gravity currents with solidifying crust, *J. Fluid Mech.* 221 (1990) 485–509.
- [29] R.C. Kerr, Melting driven by vigorous compositional convection, *J. Fluid Mech.* 280 (1994) 255–285.
- [30] C.S. Miner, N.N. Dalton, *Glycerol*, Reinhold, New York, 1953, 460 pp.
- [31] H.S. Carslaw, J.C. Jaeger, *Conduction of Heat in Solids*, Clarendon Press, Oxford, 1986, 510 pp.
- [32] N. Petford, R.C. Kerr, J.R. Lister, Dike transport of granitoid magmas, *Geology* 21 (1993) 845–848.
- [33] A.A. Arzi, Critical phenomena in the rheology of partially melted rocks, *Tectonophysics* (1978) 173–184.
- [34] K.V. Cashman, Relationship between plagioclase crystallization and cooling rate in basaltic melts, *Contrib. Mineral. Petrol.* 113 (1978) 126–142.